Contents lists available at ScienceDirect

Renewable Energy

Experimental and multiphase modeling of small vertical-axis hydrokinetic turbine with free-surface variations

Ahmed Gharib Yosry [a,b,*], Eduardo Álvarez Álvarez [c], Rodolfo Espina Valdés [c], Adrián Pandal [a], Eduardo Blanco Marigorta [a,**]

[a] GIFD Group, Energy Department, University of Oviedo, C/ Wifredo Ricart s/n, Gijon, Spain
[b] Mechanical Power Department, Faculty of Engineering, Port Said University, Egypt
[c] Hydraulic R&D Group, EP Mieres, University of Oviedo, Mieres, Spain

ARTICLE INFO

ABSTRACT

Vertical-axis hydrokinetic turbines are promising option to harness the low velocity currents. However, limited investigations have been carried out considering the interactions between the turbine rotor and the channel section, including the free-surface. Thus, a vertical-axis turbine model has been designed and manufactured, to be tested in an open channel. Also, a three-dimensional multiphase simulation has been carried out, using the volume of fluid (VOF) model, to capture the air–water interface and to investigate the free-surface variations effects on the turbine output. Experimentally, the turbine model has been characterized under different flow conditions and free-surface levels. The peak power coefficients are found to increase with the upstream velocity. This effect is directly linked to the blockage ratio and the Froude number. A reasonably good match has been found between the experimental and the numerical results. The VOF model is able to simulate the free-surface longitudinal variations, and the effect of the turbine blockage of the channel. The velocity field and the pressure coefficient distribution, around the turbine rotor, have been studied and correlated with the free-surface variations from upstream to downstream of the turbine. Finally, the vortex street generated by the blade–plate interaction has been analyzed.

1. Introduction

Hydrokinetic turbines transform the kinetic energy available in water currents into a useful mechanical work [1]. Based on the alignment of the rotor axis with respect to the water flow, three generic categories can be defined; the first one is the horizontal-axis turbines, alternately called axial-flow turbines, which have the axes parallel to the fluid flow and employ propeller type rotors. The second category is the cross flow turbines, known as "floating waterwheels", in which the rotor axis is orthogonal to the water flow but parallel to the water surface, and are based on the hydrodynamic drag. Finally, the Darrieus type or vertical-axis turbines, whose axes are also perpendicular to the fluid flow, but working on the hydrodynamic lift, and are usually derived from the rotor designs of the wind industry [2].

Among these types, vertical-axis turbines are considered a viable choice to harness the energy in the water current, particularly for low flow velocities, due to its simple design and insensitivity to the flow direction [3]. However, within the blue economy, as a more restricted

markets are exploited, continued innovation of these kind of turbines is necessary to ensure their competitiveness with other types [4].

Many investigations have been carried out to optimize and enhance the design parameters of the vertical-axis turbine, including the number of blades [5], the profile type [6] and the aspect ratio value [7]. Of the vertical-axis turbine types, the lift-based ones give the highest peak performance, specifically the straight bladed turbines. However, one of the handicaps of this turbine category is the limited self-starting capability. Increasing the turbine solidity (which is calculated as $\sigma = n \cdot C/R$, where n is the number of blades, C is the chord length and R is the radius of the turbine rotor) is the simplest solution offered to overcome this issue [8]. However, high solidity profiles cause a low power efficiency, specifically at low Reynolds number condition. To overcome this issue, the blade pitch control is applied and tested for high solidity straight-bladed turbines [9], in which the maximum power coefficient increases by 78%. Another variable pitch techniques based on the double-disk multiple stream-tube are also applied [10,11]. The flexible-high solidity foil offers a self-starting capability at water

Nomenclature

B	Blockage ratio
C	Blade chord length, m
C_p	Power coefficient
D	Turbine diameter, m
d_s	Shaft diameter, m
Fr	Froude number, $Fr = U/\sqrt{gh}$
H	Blade height, m
h	Upstream water height, m
N	Rotational speed, rpm
n	Number of blades
P	Power output, W
Q	Water flow rate, m^3/s
R	Radius of rotor, m
T	Torque, N m
σ	Solidity
A	Turbine cross-sectional area, m^2
λ	Tip speed ratio, $\lambda = \Omega \cdot R/U$
Ω	Angular velocity, rad/s
U	Upstream velocity, m/s
ρ	Water density, kg/m^3
α	Water volume fraction
V_w	Water volume, m^3
V	Mixture volume, m^3
μ	Dynamic viscosity, pa.s
g	Gravitational acceleration, m/s^2
Γ_σ	Surface tension, N/m
C_T	Instantaneous torque coefficient
y^+	Non-dimensional wall distance
Z^*	Normalized water height
L	Channel maximum depth, m
ζ^*	Normalized vorticity, $\zeta^* = \nabla \vec{u}/[u \cdot c]$
θ	Azimuth angle, degree

velocity of 0.5 m/s and above with a power coefficient value reaches to 0.37 for vertical-axis tidal turbines [12]. Hybridization between two different turbines [13] is also one of the effective solutions, Govind [14] proposes a novel strategy to combine 12 kW NREL horizontal-axis turbine with 10 kW H-type vertical axis rotor on the same tower. The excess torque from the horizontal rotor is transferred to the vertical rotor through a continuously variable transmission.

The optimization studies of vertical-axis turbines are very diverse. For instance, with respect to improving the efficiency, Villeneuve et al. [15] predict and assess the efficiency and the power output of a vertical axis turbine using a novel three-dimensional numerical model, which evaluates the potential of the detached end plates. The turbine with circular plates is 31% more efficient than the one without ending plates. With respect to the blade profile and size, among the many researches in this field, it is worth mentioning the one by Saeidi et al. [16] which applies the double–multiple stream tube modeling along with the blade element momentum theory to optimize the design of the same turbine. Otherwise, the performance of a V-shaped blades rotor has been studied numerically to improve the power output at moderate tip speed ratios, obtaining a noticeable delay of the flow separation [17]. In another instance [18], the power output from a two-blades vertical-axis turbine is analytically studied by applying the Taguchi method, in which the incoming flow angle along with the tip speed ratio are found to be the most significant parameters affecting the turbine power output. Investigations have even been extended to

consider wind and waves effects on the power output and efficiency of the tidal turbines [19].

However, one of the fundamental needs for improving and optimizing these turbines is the availability of effective analytical and numerical calculation tools. On a basic level, different theoretical approaches have been developed to define the actuator disc model in an open channel flow, taking into account the Froude number and the free-surface drop behind the turbine [20] and also the mixing zone downstream [21]. Additionally, the models have been extended to include these effects on the power output from a turbine array [22]. Moreover, the analytical tools have been applied as a sub-correction model to evaluate the power available to a turbine array through Depth-averaged simulations [23], as an alternative to the expensive three-dimensional simulations of turbine farms.

On the numerical level, investigations based on the single-phase flow analysis and without considering the free-surface effects, have been carried out to study the flow field around the hydrokinetic turbines. Typically, these studies solve the Navier–Stokes equations in a domain where the free surface is fixed, using sliding mesh to simulate the turbine rotation, and RANS turbulence models. It is unusual to find research using LES methodology, however it is sometimes employed for specific purposes. For instance, [24,25] use this model to study in more detail the turbine wake, and [26] to look for the effect of the solidity related to the flow separation at the blades. Regarding the simulation of the turbine, as mentioned above, the method that often gives the best results is the sliding mesh technique. The moving reference frame (MRF) is not usually enough due to the important interaction between the blades and the walls. Although other systems have been applied, such as the immersed boundary [27]. One of the most interesting issues in this type of simulations is the effect of the blockage that results from placing the turbine in a channel of limited dimensions, either as an isolated turbine [28,29], as a turbine farm [30,31] or even using flow acceleration elements [32]. In general, the blockage and associated procedures show a remarkable increase in turbine performance.

Nevertheless, such models are not sufficiently realistic, to accurately assess the performance and characterize the flow field of hydrokinetic turbines in open channels, because they do not consider the change of the free-surface in their analysis. For instance, Nishi et al. [33] have found that the single-phase simulation of an axial-flow turbine, in a shallow water channel, over-predicts the turbine output by a factor of 2.0 with respect to the multiphase and the experimental results. The multiphase investigations can be grouped basically depending on the topology of the turbines studied. With respect to horizontal axis turbines, it has been studied, among other things, the effect of the closeness to the walls and the free surface on the turbine performance [34, 35], the wake recovery [36], the drop of the free surface behind the rotor [37] or the influence of the proximity to the critical Froude number [38]. There are also studies related to collection devices aimed at increasing the power output [39]. Regarding non horizontal-axis turbines, multiphase investigations of Savonius type turbines [40] and cross-flow ones [41] have focused on exploiting the free-surface simulation to obtain the optimal depth position. Although sometimes, as in the last mentioned article, there is also an in-deep study on the velocity and the pressure fields. Also, in relation to the Darrieus type turbines, the topology with the horizontal-axis (perpendicular to the current), has been the most studied. As before, the influence of the depth [42] and the submersion [43] has been particularly investigated. Some researches have been carried out on the Darrieus turbines inside open channels and their interaction with the free-surface, however this investigations address only the turbine in its horizontal position [42,43].

The main objective of the present study is to characterize experimentally and numerically the performance of a small vertical-axis turbine under different flow and free-surface conditions. Also, an intensive three-dimensional multiphase simulation has been carried out to understand the complex free-surface flow field around the turbine rotor and to clarify its influence on the turbine output. Experimentally, the

Table 1
Turbine rotor specifications.

Parameter	Specification
Rotor diameter (D)	0.15 m
Rotor height (H)	0.15 m
Blade profile	NACA-0015
Chord length (C)	0.05 m
Solidity (σ)	2
Number of blades (n)	3
Shaft diameter (d_s)	0.01 m
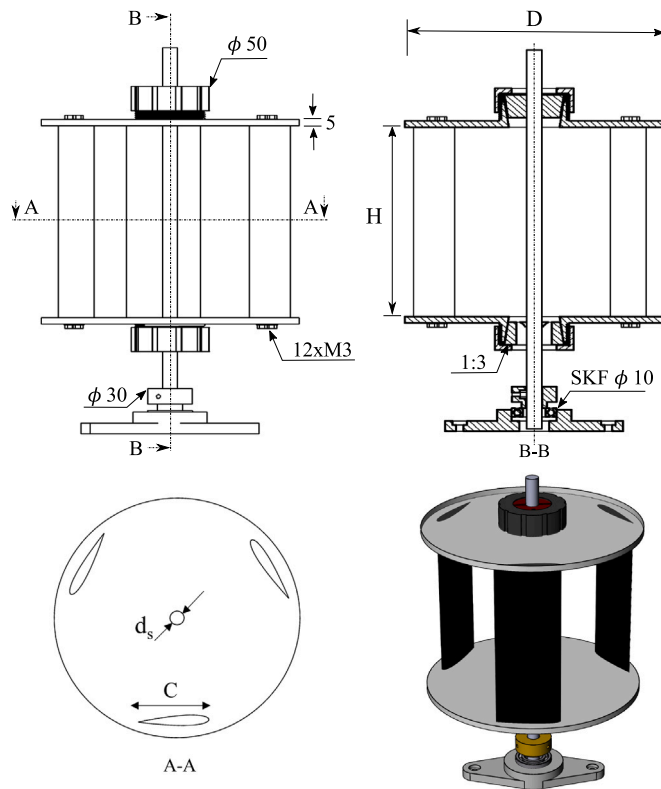
Fig. 1. A detailed schematic of the turbine model.

Fig. 2. Turbine model and fabrication process.

turbine model design and fabrication aspects are presented. In addition, the experimental test rig including the instrumentation is explained in detail. Numerically, the volume of fluid (VOF) model is used to track the free-surface air–water interface, and the sliding mesh technique is employed for the rotation of the turbine. The numerical model is validated against the experimental findings.

2. Model design and fabrication

A vertical-axis turbine model has been designed and fabricated. It is basically formed by three straight blades with NACA-0015 profile. The detailed schematic in Fig. 1 shows also the two ending plates, shaft-gripping system and ball bearing support. The geometrical parameters of the turbine model are provided in Table 1. These parameters have been carefully selected in order to obtain a self-starting and efficient operation. Specifically, the NACA-0015 symmetrical airfoil has been chosen due to its good hydrodynamic performance at low Reynolds number [6] and under different free-surface effects [44]. The thickness has been selected based on a comparison between different symmetrical airfoils under low flow velocity conditions [45]. Additionally, the ratio between the turbine height to the diameter (aspect ratio) has been set to 1.0, which has been found to enhance the performance of small turbines under confined conditions [46].
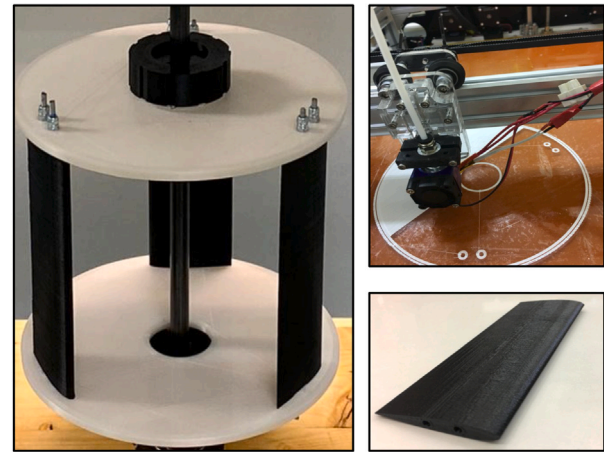
Regarding the self-starting issue, a high blade solidity has been selected as the most practical and effective solution for the low starting torque. A blade chord of 0.05 m has been chosen, resulting in a solidity value of 2.0 [7]. The experimental and numerical tests have been carried out at a Reynolds number (based on the upstream velocity and the blade chord) value around 2.5×10^4. This value is somewhat small compared with those in real applications. However, for large scale prototypes, the performance of lift-based turbines is usually enhanced due to the better characteristics of the NACA-0015 blade profile at higher Reynolds values [47,48]. So, larger turbines will have usually better self-start and efficiency characteristics than the studied model at the same upstream velocity. Finally, the proposed model has two ending plates of 0.15 m in diameter and 0.05 m in thickness to support the turbine blades and improve the hydrodynamic performance through reducing the blade tip vortices and the flow in the span-wise direction [5].

The model is designed using 3D-CAD software and manufactured with the FDM (Fused Deposition Modeling) printing technology using Polylactic acid (PLA) material for its flexibility and high strength. The turbine components have been mounted on a steel shaft of diameter (d_s = 10 mm) using a slotted-chuck mechanism, allowing the turbine to be positioned at different heights. Fig. 2 shows a photo of the turbine model and its fabrication process using the additive technology.

3. Methodology

3.1. Experimental methodology

Experimental tests have been carried out in an open water channel facility to evaluate the performance of the small vertical-axis turbine under low flow velocity conditions, and to validate the multiphase flow analysis. The water channel system (Fig. 3) consists of: a rectangular-section glassed channel, with recirculation tanks, pumps and control gate. Also, it contains a brake-torque measuring system governed by a control and data acquisition (SCADA) set-up.

The channel is 1.5 m long and has a rectangular section of 0.3 x 0.5 m with water velocity in the test section ranging between 0.14 m/s and 0.9 m/s, and with a height regulated by a control gate at the discharge of the channel. The flow is achieved by two 15 kW centrifugal pumps, with a combined nominal flow rate of 600 m^3/hr, with a variable velocity frequency regulation. The brake-torque measuring system has a high precision torque and rotational speed sensor, combined with a hysteresis brake (Magtrol TS103 and Magtrol HB-140M-2 respectively, with a precision of 0.1% in the torque and 0.015% in the rotating speed). The turbine is connected to the measuring system
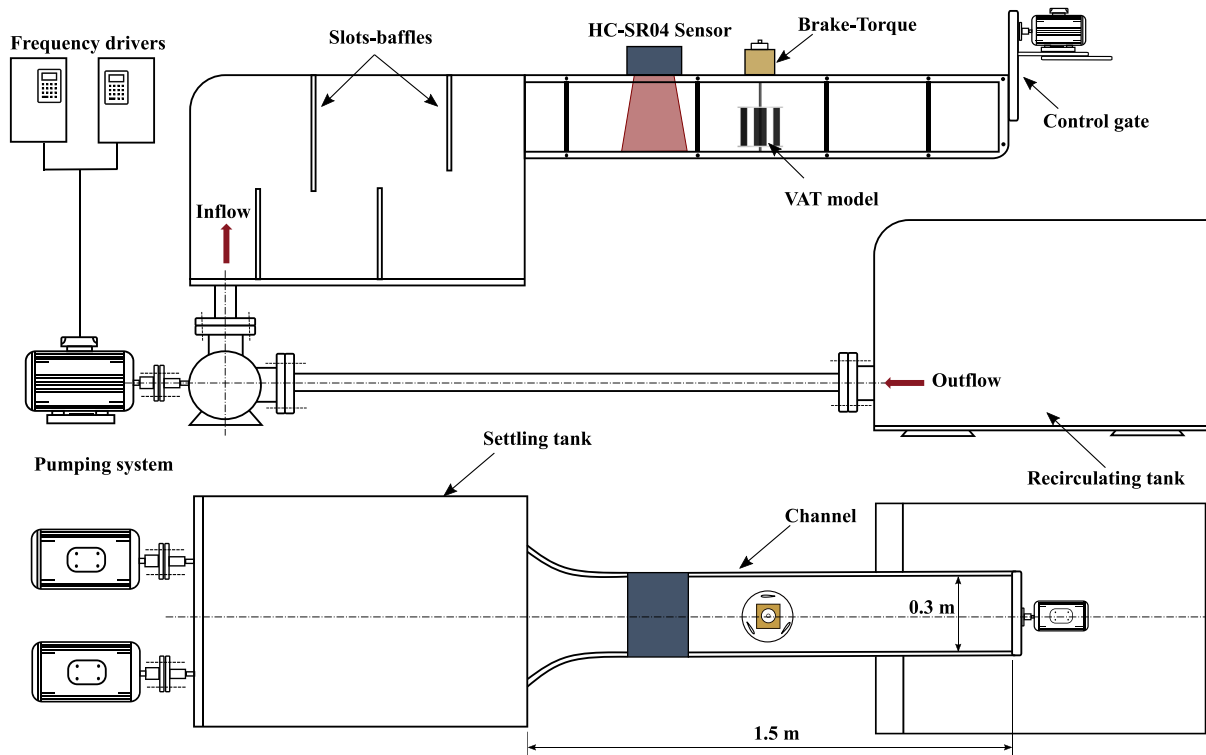
Fig. 3. The experimental test rig.

mechanically through two flexible couplings. The water height of the channel is measured with three ultrasonic sensors (HC-SR04, precision of 0.001 m) through the width of the channel. The water height is also measured in the high speed (1000 fps) videos recorded to monitor the rotation of the turbine. Due to the surface fluctuations, the uncertainty of the water average height measurements has been estimated between 0.7% and 1.1%.

In the experiments, the mechanical torque is measured together with the rotational speed N, the water flow rate Q, and the upstream water height h. From these values, the turbine power output and power coefficient $C_P = P/(0.5 \cdot \rho \cdot A \cdot U^3)$ are calculated in function of the tip speed ratio $\lambda = \Omega \cdot R/U$ (ratio between the tangential velocity of the blade tip and the upstream flow velocity). Three flow rates are used in the experiments: $Q_1 = 0.05$ m³/s, $Q_2 = 0.06$ m³/s and $Q_3 = 0.065$ m³/s. For each flow rate, different flow conditions are obtained using the control gate, ranging from the lowest applicable velocity up to the maximum possible velocity (critical flow condition at channel outlet). From these values, five upstream flow velocities are selected for each flow rate within the range from 0.33 m/s to 0.69 m/s.

3.2. Numerical methodology

3.2.1. The model

A three-dimensional multiphase analysis – considering the water free-surface – has been performed using ANSYS FLUENT software to simulate the turbine model. From the experimental results, three different cases have been selected for the simulation. The first case (C_1) in which the channel is fully-filled with water and the control gate is slightly opened, with an upstream velocity value of 0.43 m/s; the second case (C_2) with an intermediate opening and an upstream velocity value of 0.57 m/s; finally, the third case (C_3), where the control gate is fully opened and the upstream velocity value reaches 0.69 m/s. In addition, for the first case configuration, a single-phase three-dimensional simulation, without considering the free-surface, has also been carried out for comparison with the multiphase results, to examine the effect of the free-surface on the turbine output.

The volume of fluid (VOF) method developed by Hirt and Nichols [49] is applied in the present simulation to model the free-surface (air/water interface). It has been selected for its capability of reproducing and capturing the free-surface deformation accurately under different flow conditions. For this method, the water volume fraction is defined as $\alpha = V_w/V$, where V_w is the water volume in the cell and V is the total volume of the mixture. The physical properties of the air–water multiphase fluid can be calculated as:

$$\rho = \alpha \cdot \rho_w + (1 - \alpha)\rho_a \tag{1}$$

$$\mu = \alpha \cdot \mu_w + (1 - \alpha)\mu_a \tag{2}$$

where ρ and μ are the mixture density and dynamic viscosity respectively. A value of $\alpha = 0.5$ represents the free-surface location. The VOF governing equations are the mass, momentum and volume conservation equations. The VOF model assumes that the pressure and velocity fields are the same for both phases and solves a single momentum equation [Eq. (3)].

$$\rho \frac{\partial \vec{u}}{\partial t} + \rho \cdot \nabla(\vec{u} \cdot \vec{u}) = -\nabla p + \mu \cdot \nabla^2 \vec{u} + \rho \cdot \vec{g} + \Gamma_\sigma \tag{3}$$

where u and p are velocity and pressure field respectively, $\vec{g}$ is the gravitational acceleration vector and Γ_σ is the surface tension term. In this approach, the tracking of the interface between the fluids is accomplished by solving the volume fraction continuity equation for each of the phases excluding the reference one [Eq. (4)].

$$\frac{\partial}{\partial t}(\alpha \rho_w) + \nabla(\alpha \rho_w \vec{v}) = \sum_{w=1}^{k-1} \gamma_{w \to a} \tag{4}$$

where a and w refer to the reference phase (air) and the secondary phases (in this case is only one, water), k is the total number of phases, and $\gamma_{w \to a}$ is the mass flow rate per unit volume from each secondary phase to the reference one.

3.2.2. Computational domain

The computational domain is divided into two main regions: the inner domain, which includes the turbine model and corresponds to
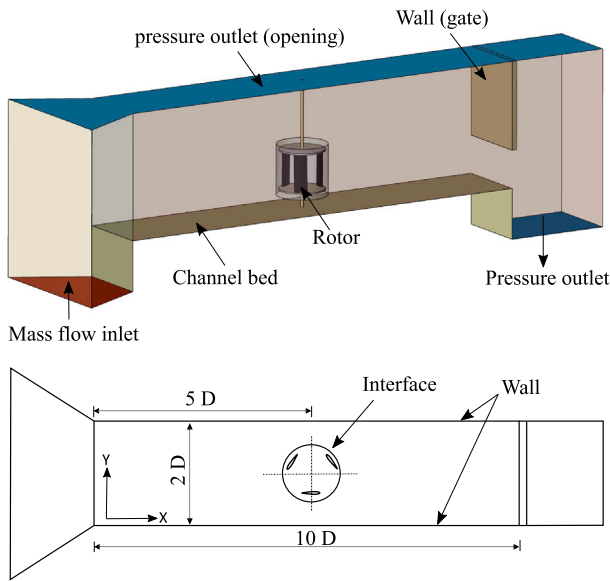
pressure outlet (opening)

Wall (gate)

Rotor

Channel bed

Pressure outlet

Mass flow inlet

5 D

Interface

Wall

2 D

Y

X

10 D

Fig. 4. Computational domain.

the rotating region, and an outer domain for the rest of the channel corresponding to the stationary region. A sketch of the computational domain including the boundary conditions is shown in Fig. 4.

The domain dimensions are based on the hydrodynamic channel size used in the experimental tests, which covers 10 times the turbine diameter in length and a double diameter in width. A mass-flow inlet boundary condition has been applied to the upstream side of the channel domain, while a zero pressure-outlet boundary condition has been selected for the downstream exit. The interface region includes the simulated turbine which is located at the center of the channel region. A sliding-mesh technique has been used between these two zones, keeping the meshes connected during the different angular positions for each time-step. The turbine blade surfaces and the channel walls have no-slip wall boundary conditions. The upper surface has a pressure outlet boundary condition in the multiphase simulation cases and a zero-shear stress boundary condition in the single-phase simulation. Also, the control gate in the multiphase simulations has no-slip wall boundary and its position is changed for each simulated case.

The whole domain has been discretized using a fully structured mesh with hexahedral shaped cells. Fig. 5 illustrates the details of the computational grid for both of the turbine rotor and the channel. Three mesh sizes (*L*, *XL* and *XXL*) have been used to check the mesh quality as listed in Table 2. A refinement factor (RF) has been applied around the turbine blades, keeping the first layer height around the blades constant at 1.2×10^{-5} m from the wall surface, resulting in a maximum non-dimensional wall distance (y^+) of 0.7. This value is acceptable to resolve the viscus sub-layer as recommended by the transition turbulence models.

3.2.3. Grid quality evaluation

The Grid Conversion Index (GCI) method developed by Roache [50] has been applied to test the mesh refinement. It is based on the generalized Richardson extrapolation, involving comparison of discrete solutions in two different spacing meshes. In the current study, the GCI method has been performed for the three meshes in Table 2, using the torque coefficient as the reference value, with a recommended safety factor of 1.25 [50], and a calculated order of convergence value of 3.0. The results of the static torque coefficients and the convergence rates for the three simulated meshes are also presented in the table. The GCI_{12} has been found to be 0.172%, while the GCI_{23} has a value of 0.018% with the asymptotic convergence value of 0.935. This

Table 2
Mesh quality analysis.

Size	Rotor volumes	Total volumes	C_T	Error %	GCI %	RF
Coarse, *L*	503,622	1,005,3727	0.247	–	–	0.5
Baseline, *XL*	889,800	1,391,550	0.2581	0.1719%	4.2%	1
Fine, *XXL*	1,720,200	2,221,950	0.2593	0.0187%	0.4%	2

corresponds to 0.4% change in the torque coefficient value when the mesh is refined from *XL* to *XXL*, indicating that further refinement of the baseline mesh has small influence on the output results.

The Reynolds Averaged Navier–Stokes equations (RANS) is solved using the shear stress transport (k-ω SST) turbulence model developed by Menter [51]. This model combines a robust formulations of the near-wall taken from the k-ω Wilcox model [52] with the far-wall k-ε model, through a blending function that ensures a smooth transition between both.

To initiate the simulation, a steady flow calculation is performed to fill the water channel using the same parameters corresponding to the experimental test case (mass flow inlet and control gate height). After the steady simulation process stabilizes and converges, the reference water height obtained from this preliminary simulation is verified with the experimental one. Subsequently, a transient simulation is carried out, in which the time step size corresponds to the time required to move the rotor one small fraction of a turn. Fig. 6, compares results obtained with different degrees/time-step values. It has been found that decreasing the degrees/time-step below 1°/step has a negligible influence, (only 0.38% for 0.5°/step). Thus, that value has been applied as a good trade-off between accuracy and computational cost.

The time step convergence criterion has been set for all parameters at 10^{-6}. The overall convergence criterion is based on the variation of the averaged torque coefficient value over a complete revolution between two successive cycles. At the beginning of the solution, starting instabilities have been observed followed by a transient phase (Fig. 7). To achieve a periodical solution with a variation of less than 1% between two subsequent cycles, 28 numerical revolutions have been calculated, even if the solution usually stabilizes earlier.

4. Results and discussion

In this section, the results from the experimental testing and multiphase numerical simulations are used to assess the performance of a small vertical-axis hydrokinetic turbine in an open water channel. The parameters analyzed include the upstream velocity, the Froude number and the free-surface variations.

4.1. Experimental performance characteristics

Experimental tests have been carried out for three flow rates, with several flow conditions (upstream velocities) for each one. The power produced by the turbine has been plotted in Fig. 8. At the top, the power is presented as a function of the rotational speed, while the bottom shows the dimensionless power coefficient as a function of the tip speed ratio. Results have been obtained corresponding to five upstream velocities per flow rate.

For each upstream velocity, the maximum rotational speed corresponds to the zero-load condition. By increasing the turbine load, the rotational speed decreases until it reaches the maximum power point (MPP). From that point on wards, the power output from the turbine decreases with the decline of the rotational speed, which makes this part of the curve unstable. It can also be observed that, by increasing the upstream velocity values, the power output increases and the rotational speeds are shifted to higher values. Similarly, the same trend has been obtained for all upstream velocities, except for the flow rate Q_1 at a velocity of 0.61 m/s. For this flow condition, the water level at the upstream side is nearly at the same elevation as the turbine top
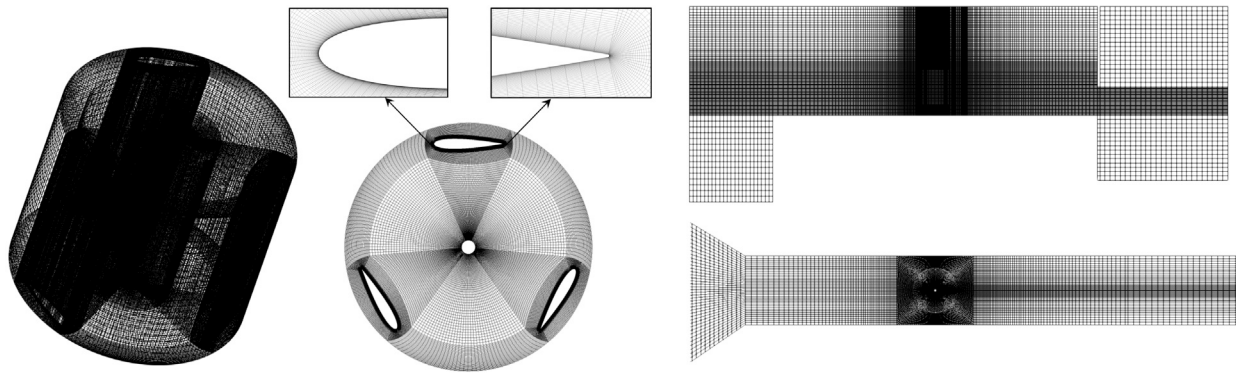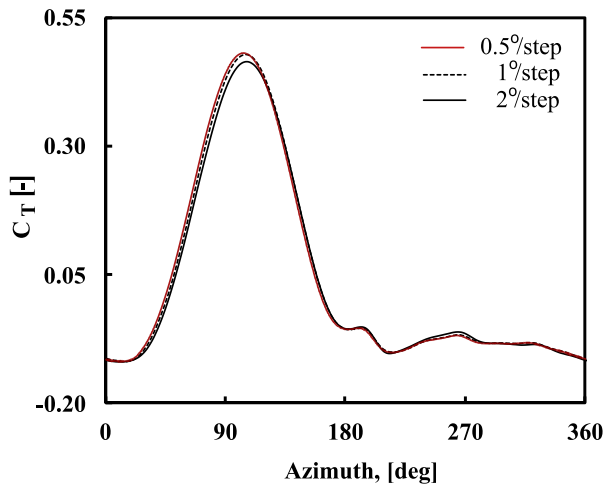
Fig. 5. Computational grid.

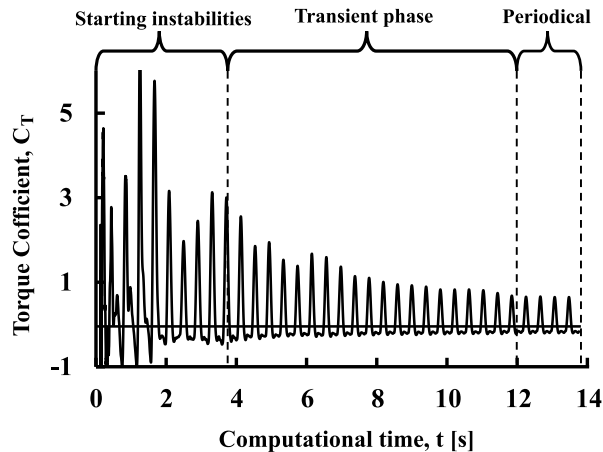**Fig. 6.** Torque coefficient for different time-step values at $\lambda = 2.6$.

Fig. 7. Numerical calculations of the torque coefficient of a single blade over 28 cycles.

plate and, due to the water surface drop in the downstream side, the backside of the rotor is exposed to the air.

The characteristics of the vertical-axis turbine are traditionally expressed in terms of the non-dimensional parameters tip speed ratio λ and power coefficient C_p, to better compare the performance at different flow rates and upstream velocities. For an ideal turbine operating in an open field (with no blockage effect), those curves should be identical, but for a non-ideal turbine operating in a confined channel,

the characteristic curves have significant differences (Fig. 8). For each flow rate, the peak power coefficient increases with the upstream velocity. This effect is related to the blockage ratio. When the channel is fully filled with the flow, the turbine model occupies 15% of the channel cross-section. This condition is achieved at the smallest practical velocity for all flow rates. To increase the upstream water velocity, for a fixed flow rate, the water height has to go down, increasing the blockage ratio up to a maximum value of 23.8%.

In fact, the Froude number (ratio between characteristic flow velocity to gravitational wave velocity) plays an important role on the power obtained because it combines the effect of upstream velocity and blockage. It is calculated from $Fr = U/(gh)^{0.5}$ where g is the gravitational acceleration and h is the water height. The effect of the upstream Froude number on the maximum power output MPP for different flow rates is shown in Fig. 9. The Froude number has been varied over a subcritical range of [0.15–0.38] by changing the gate height for different flow rates, giving the aforementioned blockage ratio range of [15%–23.8%]. By increasing the Froude number, which implies an increase in the upstream velocity and a decrease in the upstream water height, the maximum power output from the turbine rotor increases. In the figure it can be seen that, for the higher flow rates (Q_2 and Q_3), the influence of the Froude number on the power is practically linear. However, the lower flow rate Q_1 shows a quite different behavior even with a drop of the maximum value. As mentioned above, this is mainly due to the interference of the free-surface with the turbine.

4.2. Numerical model validation

In the present study, the numerical model has been validated with the experimental data in two steps; the first one is by comparing the turbine characteristic curve, that is obtained experimentally, with the multiphase and single-phase simulations for the first case (C_1) as shown in Fig. 10. The second validation method compares the free-surface from the experimental tests with those obtained from the multiphase simulation of the three cases C_1, C_2 and C_3 as illustrated in Fig. 11 and in Fig. 12.

With respect to the turbine characteristic curve, the comparison case C_1 corresponds to the maximum flow rate Q_3 and an upstream velocity of 0.43 m/s, with the channel nearly overflowing. A reasonably good match has been found between the experimental and the numerical results for the whole range of tip speed ratios (Fig. 10). Single-phase and multiphase simulations show the same tendencies as the experiments, confirming that the main flow physics are correct in both of them. However, the single-phase model values are somewhat higher than the experimental ones. Most likely because this numerical model does not consider the free-surface deformations found in actual reality, specifically the change in the free-surface level around the rotor when the power is extracted from the turbine. In fact, the difference between the single-phase model and the experiments tends to increase with the
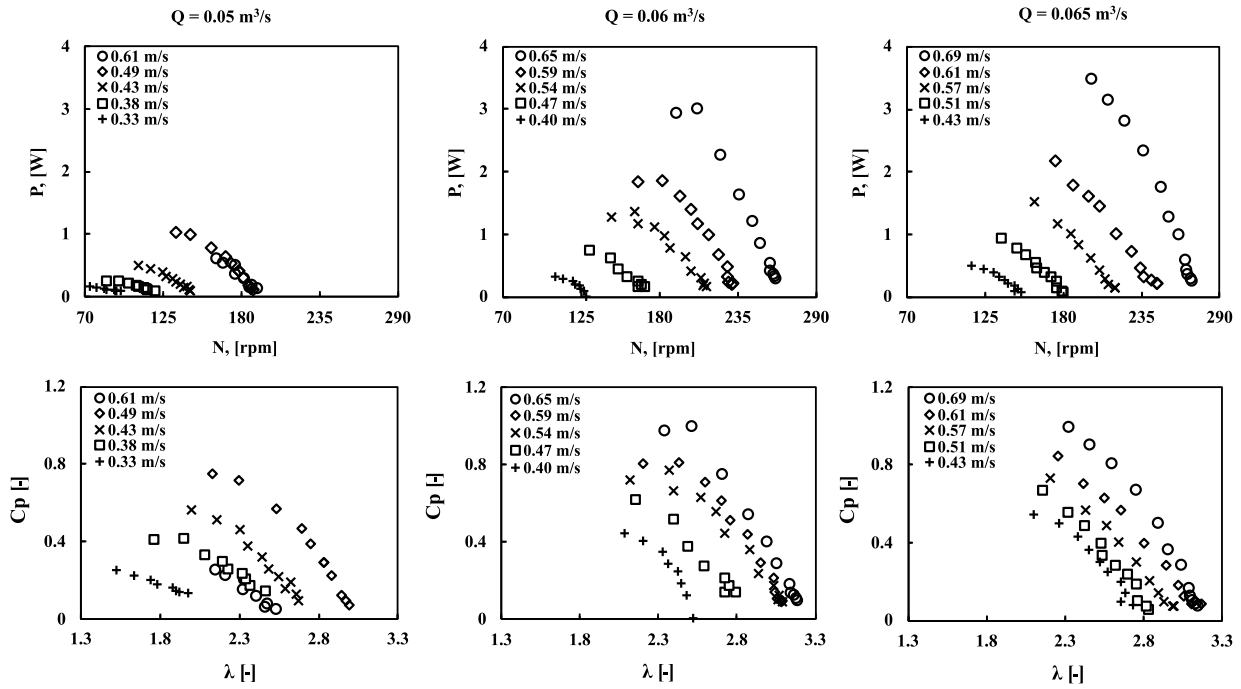
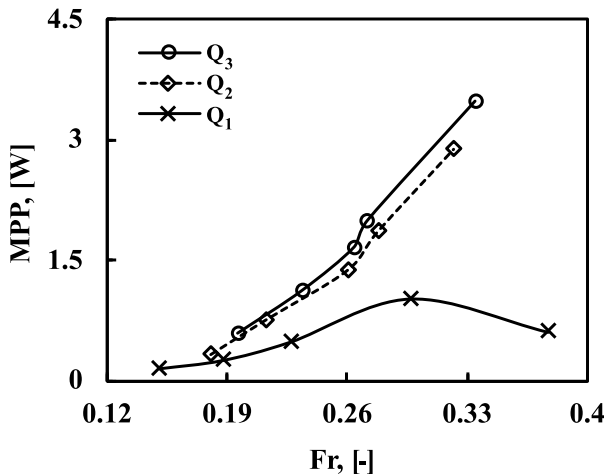**Fig. 8.** Power and characteristic curves for different upstream velocities.

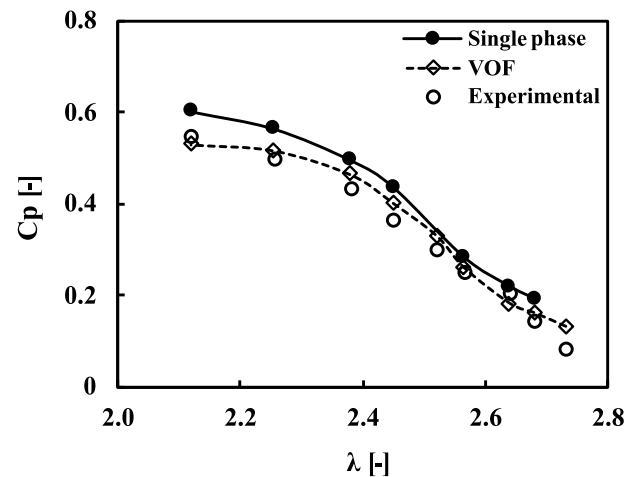**Fig. 9.** Variation of MPP with the upstream Froude number for different flow rates.

Fig. 10. Characteristic curve validation for (C_1).

power extracted (as the tip speed ratio decreases). By considering the free-surface variations, the VOF model obtains power coefficients much closer to the experimental measured ones for the whole range of the tip speed ratios.

Regarding the free-surface comparison between the experiments and the VOF model, three cases have been selected, corresponding to the highest flow rate Q_3 and the tip speed ratio of $\lambda = 2.3$, but with different upstream velocities. Fig. 11 shows the comparison of the free-surface levels at the middle of the channel for the three cases C_1, C_2 and C_3. The results are quite consistent in all of them, following the free-surface variations even when the flow becomes supercritical as in the C_3 case.

Although in a more qualitative mode, Fig. 12 shows the three-dimensional shape adopted by the free-surfaces, comparing the results of the VOF model with the experiments. The VOF model is able to simulate not only the longitudinal variations, but also the interactions with the channel wall boundaries. In C_1 case, it can be observed that

there is a slight decrease of the free-surface just after the turbine, which recovers quickly. In the C_2 case, the drop after the turbine is deeper, corresponding to a higher energy extraction. The subsequent recovery is also more abrupt and turbulent, although the original level is also recovered. In both cases, the free-surface drop is quite smooth covering the whole width of the channel, while the recovery shows more disturbances and wave reflections from the channel walls. In the C_3 case, corresponding to the maximum inlet velocity, the energy extraction is also the highest, which requires the flow to go from a subcritical regimen before the turbine to a supercritical one after the turbine.

4.3. Performance and flow field analysis

The torque produced by the turbine is the sum of each blade contribution. The numerical model enables to easily visualize the variations
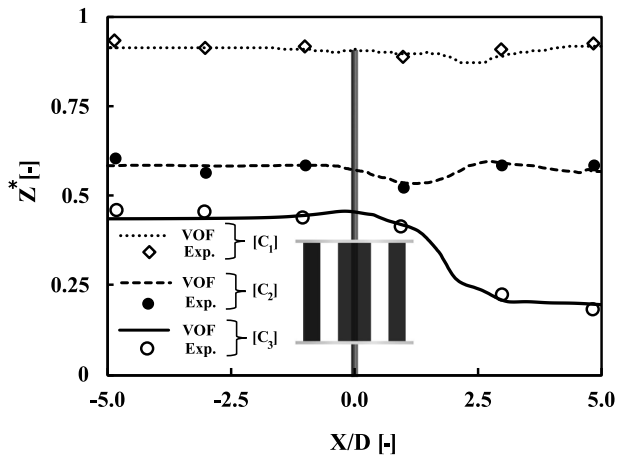
Fig. 11. Free-surface validation with the experimental normalized heights ($Z^* = h/L$) at $\lambda = 2.3$.

produced during each revolution of the rotor and even the effect corresponding to each blade. For instance, Fig. 13 shows the polar distributions of the instantaneous torque coefficient C_T as a three lobed rosette, corresponding to the current three-blades turbine model. The figure compares the results for the case C_1 with the single phase model against the VOF model, for two different tip speed ratios. It also shows the results for the cases C_2 and C_3 with the VOF model.

The three lobes are very clearly defined, which implicitly means that the positive effect of each blade is limited to a relatively small angular range. The peaks coincide in all cases indicating that the angular zone of maximum effect does not change with the upstream flow velocity nor the tip speed ratio, but is geometrically defined. Similar polar trend for a Darrieus horizontal axis water turbine has been reported by Le Hocine et al. [43]. The comparison between the single-phase and VOF simulation shows that the variations are more pronounced in the former, especially when increasing the tip speed ratio. For the cases of the VOF model, the three lobes are also more defined at the higher tip speed ratio, although not as much as in the single phase model.

In this kind of polar figure, the total torque coefficient of the turbine is equivalent to the area enclosed by each curve. The variation in the total torque coefficient between the two tip speed ratios is clearly seen, for instance, the total torque coefficient for the C_1 case is 0.225 for $\lambda = 2.3$ and 0.083 for $\lambda = 2.7$. The average difference between both tip speed ratios is about 52%, as the lower tip speed ratio ($\lambda = 2.3$) always producing more power. The difference in area is also evident between the three cases for each tip speed ratio ($C_3 > C_2 > C_1$). For instance, at $\lambda = 2.3$, the torque coefficient of C_2 case is 38% higher than C_1 one, while the C_3 case is 49% higher. Also the lobes are less defined as the power increases, denoting an increase in the positive angular range.

The change in the turbine output and its performance is directly related to the flow around the turbine rotor and its blades, also with the deviation caused by the deformation of the free-surface. To further explore the phenomena, the velocity vectors at the middle of two different planes for the three VOF simulated cases are shown in Fig. 14. An horizontal plane passing through the mid-height of the turbine on the left (Fig. 14a) and a vertical longitudinal plane passing through the axis of the turbine on the right (Fig. 14b).

In this figure, the wake is clearly visualized. It has different extensions in each case and it is slightly deviated towards the rotational direction of the turbine (upward in Fig. 14a). There are also zones of low velocity in front of the turbine and in the center of the rotor, where the flow slows down. Around the turbine –laterals, top and bottom– the velocities increase, more so the higher blockage (for C_1, C_2 and C_3 cases the blockage ratios are 15%, 19% and 24% respectively). Inside the

turbine and specifically in the influence zone of the blades, the velocity has also an important circumferential component due to the drag of the blades. The low velocity field around the turbine shaft is most likely due to this circumferential flow. The increase in the velocity around the turbine as a consequence of the blockage is much higher when the turbine is in a channel than in an open field condition. Moreover, the blockage and corresponding velocities increase as the height of the upstream free-surface decreases from C_1 to C_3 case. However, a feature that contrasts with the situation in the open field is the reduction of the flow cross-section downstream of the rotor. In the open field condition, the turbine blockage forces the flow around the turbine to expand until the wake is absorbed. But, as the turbine is inside a channel condition, the free-surface area in the wake zone decreases in elevation.

This has been explained, for instance, by the analytical model offered by Houlsby et al. [21], which is an extension of the Linear Momentum Actuator Disc Theory (LMDAT). In this model, the flow is decomposed into two main streams; the first one passes through the turbine rotor, loses a part of the energy, and expands behind the turbine in the wake region. The second one is the bypass zone which is formed around the turbine rotor, where no energy is extracted and a higher velocity field is developed due to the turbine blockage. The flow is accelerated in the bypass zone to conserve the mass flux in the wake region causing a reduction in the static head and consequently reducing the free-surface level. Usually, the free-surface elevation is partially recovered when the bypass zone is mixed with the wake and the velocity is equalized. However, in certain cases (if the Froude number is sufficiently high) the flow become supercritical as in C_3. Paradoxically, the wake extension is reduced as the blockage increases. The drop of the free surface is responsible for this faster wake recovery, because it can be regarded as a contraction of the flow in a nozzle. The difference in levels or more correctly in total head between the upstream and downstream zones is the energy extracted from the flow, although the energy obtained by the turbine is somewhat lower because of the losses produced in the wake. This energy extraction is directly linked to the magnitude of the velocity in the turbine, specifically around the blades. Therefore, the greater the blockage –and the deeper the free surface drop– the more power is obtained.

The wake recovery process can be analyzed in more detail as shown in Fig. 15, which presents the velocity vectors with the normalized vorticity contours (normalized with the upstream velocity and blade chord ratio $\zeta^* = \nabla \vec{u}/[u \cdot c]$) in two sectional plane views: one in the mixing zone, about one diameter behind the turbine rotor (Fig. 15a), and another one in the far-wake region, about two diameters downstream (Fig. 15b). For the three cases, in the mixing zone a low velocity wake region can be appreciated and how the flow in the bypasses around the rotor shifts to fill this area, developing two distinctive main vortices located in the wake of the turbine plates. With the wake evolution from the mixing zone to the far-wake region, these vortices coalesce in one main vortex, leaving a wake which is swirling in a clockwise direction. With the colors of the vorticity contours, it can be noticed that in the mixing zone the vortices have a high intensity and a reduced extension, while in the far-wake the main vortex has a much larger distribution but it is somewhat mitigated.

To further explore the effect of the free-surface on the blade hydro-dynamics, the relative streamlines around the turbine blade at various azimuth angular positions from $\theta = 60°$ to $\theta = 300°$ are illustrated in Fig. 16. The angles of 60° and 120° correspond to the zone where positive torque is obtained, while those of 240° and 300° are in the resistance zone. The incidence angle of the relative streamline velocity at the leading edge increases from C_1 to C_3, especially in the positive production zone, where the lift force direction increases the torque values and the hydrodynamic efficiency. In the C_1 case, the incidence angles are the lowest –very close to zero but still enough to obtain a positive torque at 60 degrees– and there is no separation at any point. This is favorable in the positive production zone but not in the rest where a noticeable resistant torque is attained. In the cases of
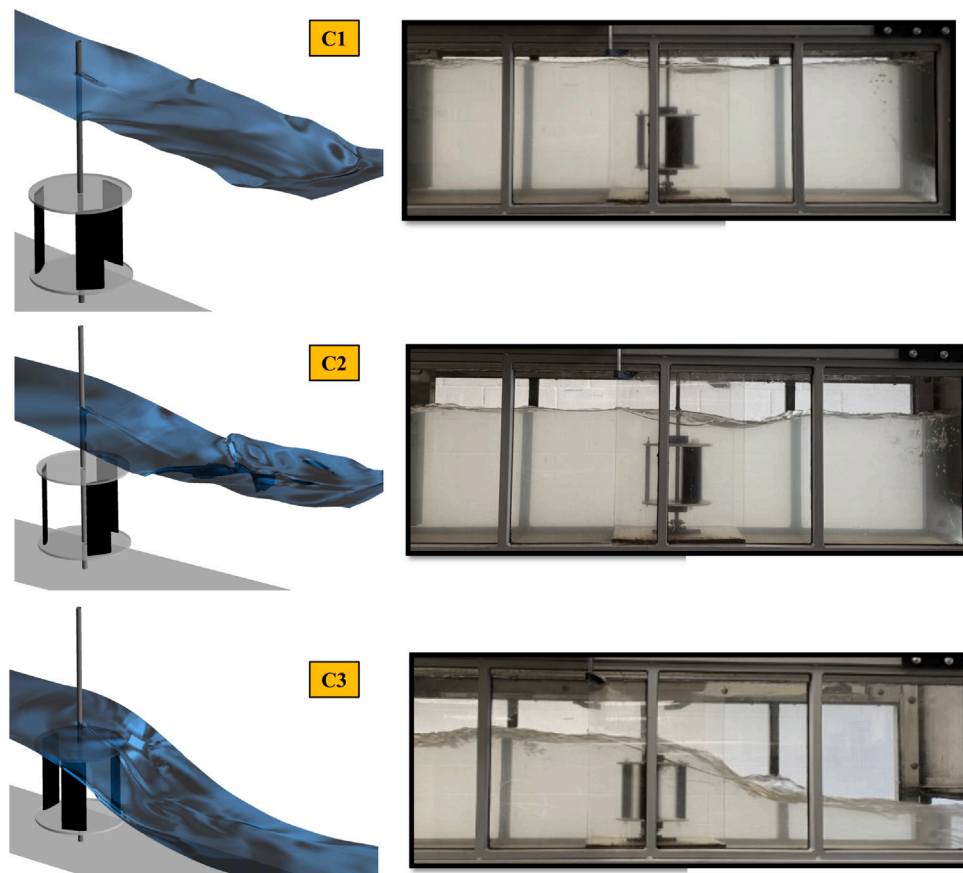
Fig. 12. Free-surface shape around the turbine rotor (isosurface water fraction of 0.5) at $\lambda = 2.3$.
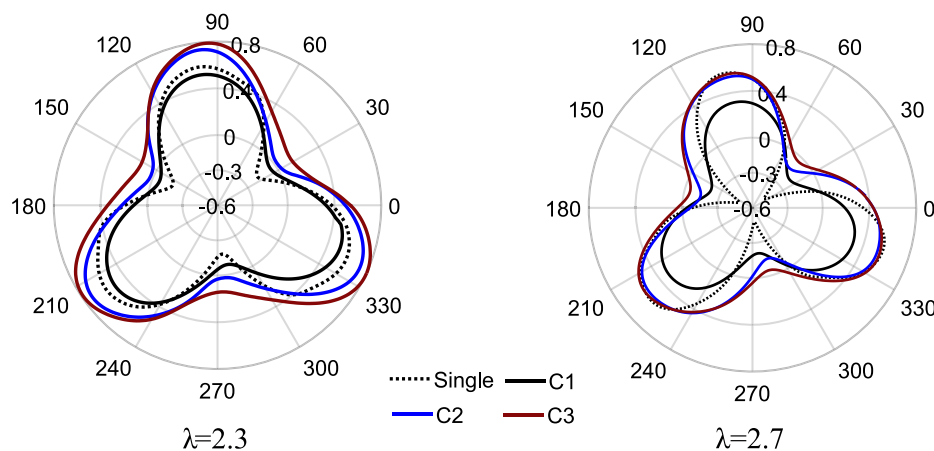

Fig. 13. The polar distributions of the instantaneous torque coefficient (single phase and VOF model cases).

C_2 and C_3, the free-surface is nearer to the turbine and the relative flow angles have a larger variation range which even leads to the flow separation. Specifically, for the C_3 case, it can be seen how the separation is quite strong with clear separation bubbles. The detachment of the flow at the angle range between 240° and 300°, reduces the forces that generate the rotation resistance, so that the torque does not even become negative in spite of the increased drag. This type of hydrodynamic stall is very specific for these cross-flow turbines but does not exist in axial ones. In the latter it has been found that the primary mechanism of the performance change is linked to the free surface deformation [34]. However, for the model in the current study, the C_3 case has extreme free-surface deformation, but the separation

is already detected in the C_2 case where the shape change of the free surface is not so pronounced. Although further study is needed, it seems that the increase of the incidence angle that generates the positive torque is quite gradual, but the separation of the flow in the resistance zone produces a sudden increase of the power obtained. This indicates that the change in performance is more related to the depth of the free surface than the change in shape.

Fig. 17 shows the pressure coefficient distribution on a single blade for different angular positions and corresponding to the three cases analyzed. A detail of the position and the pressure distribution contours for the C_2 case has been superimposed as a reference at the lower right corner. In these figures, the area between the pressure and suction sides
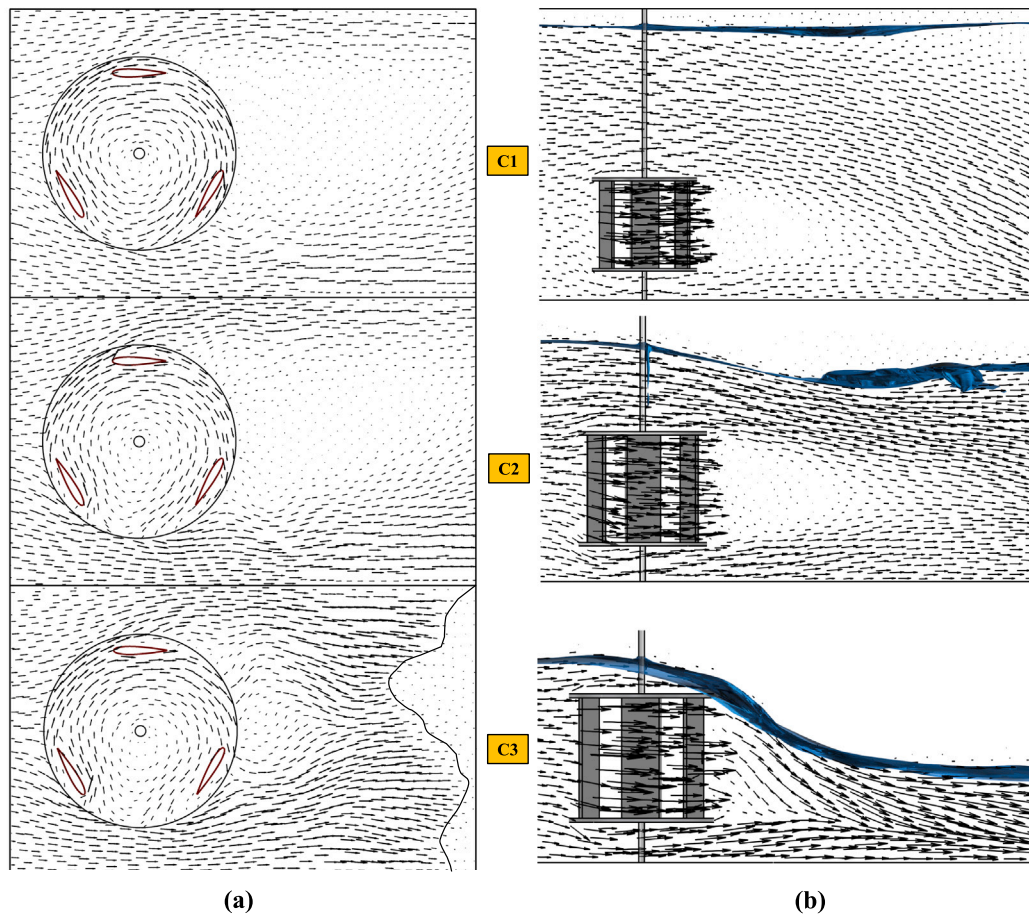
Fig. 14. Velocity vectors with Iso-surface shape ($\alpha = 0.5$) at two different planes: (a) $Z/H = 0.5$ and (b) $Y/D = 0$, at $\lambda = 2.3$.

is proportional to the lift. Normally, this area is desired to be as large as possible, but in cross-flow turbines, the scenario is complicated: the direction of the relative velocity changes substantially around the rotor, so that the velocity component contributing to the driving torque can become even negative for certain angles and flow rates.

In fact, of the angles shown in the figure, only the 60° and 120° ones are in the positive torque zone for this turbine, while the rest are in –what can be called– the resistance zone. For the former ones, the behavior is typical of an airfoil, with over-pressure on one side and under-pressure on the other. The area (lift) grows with the upstream velocity, from the C_1 to the C_3 case. For the 60°, the distribution is very smooth in all three cases as it corresponds to a smooth flow along the profile. For the 120°, in the C_2 and the C_3 cases, a separation bubble is observed near the leading edge although the flow reattaches and there is no stall. This partial separation is due to the increase of the blockage and the lowering of the free-surface from the C_1 to the C_3 case. These effects not only raise the velocity magnitude but also increase the angle of attack, which becomes very close to the limit for the 120° angle.

For the 180°, the pressure coefficient on both sides of the profile practically coincides, thanks to the similarity in the direction between the tangential velocity of the blade and the flow velocity at this position. For the rest of the angles (0°, 240° and 300°), located in the resistance zone, the pressure coefficient behavior is very different from a typical aerodynamic profile. On the face that would correspond to the pressure side, the coefficient begins with an over-pressure peak –which is expected– but then the pressure drops even below the value on the suction side. The same happens, inverted, on the other face: it starts with an under-pressure peak but then rises to even positive values. This line crossover causes a positive lift near the leading edge and a

negative one in the middle and the rear part of the blade. This abnormal behavior is due to the high blade solidity which causes a significant low pressure at the inner zone of the turbine. This effect, along with the blockage discussed above, results in a large change in the direction of the relative velocity. So large that there are areas where the torque force is effectively opposite to the motion, reducing power generation. The C_2 and C_3 cases are further complicated by the separation that causes a second crossing of the pressure coefficient lines. Normally this separation is undesirable because it decreases lift and torque but, in this case, since the torque is negative, the separation is favorable because it minimizes this negative effect.

The normalized vorticity fields around the turbine rotor are shown in (Fig. 18), at a longitudinal vertical plane on the left side (a), and at an horizontal plane passing through the mid-height of the turbine on the right side (b). In both cases, the value represented is the vorticity component perpendicular to each plane, normalized with the upstream velocity and blade chord ratio.

In the vertical plane, the vortices generated by the lower and upper turbine plates can be observed, straddling the wake behind the turbine. The intensity of these vortices and their downstream extension increase with the free-surface lowering (from C_1 to C_2), consistent with the increase in the longitudinal velocity generated by the blockage. However, in the C_3 case, the free-surface drop and the flow convergence behind the turbine produce a much faster mixing of the vortices with the central part of the wake. In the horizontal plane (Fig. 18b), the velocity component corresponds to the blades circulation and has higher values than the transverse directions. It can be clearly visualized the opposing vortices generated on the suction and the pressure sides of the profiles. In the absence of separation, these vortices extend far behind the blade in a smooth and continuous manner, until they interact with
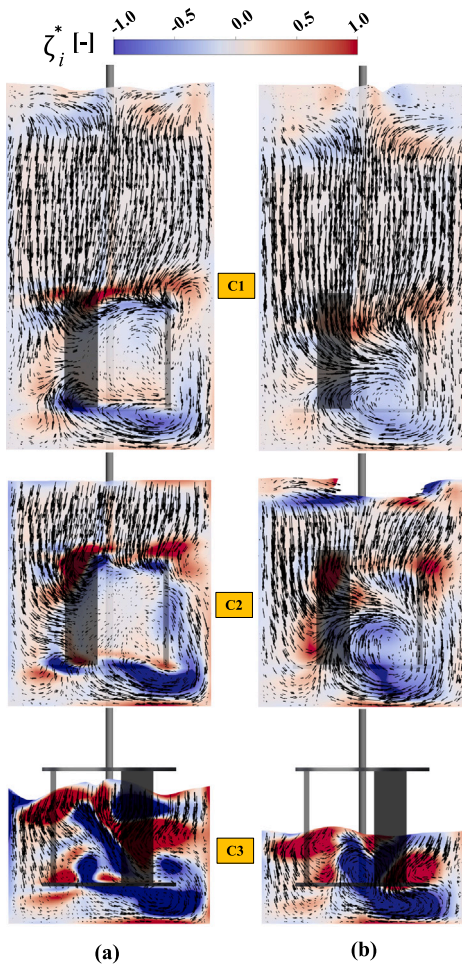
Fig. 15. Velocity vectors with normalized vorticity contours ($\zeta^* = \nabla\vec{u}/[u \cdot c]$) at two downstream planes: (a) $X/D = 1$ and (b) $X/D = 2$, at $\lambda = 2.3$.
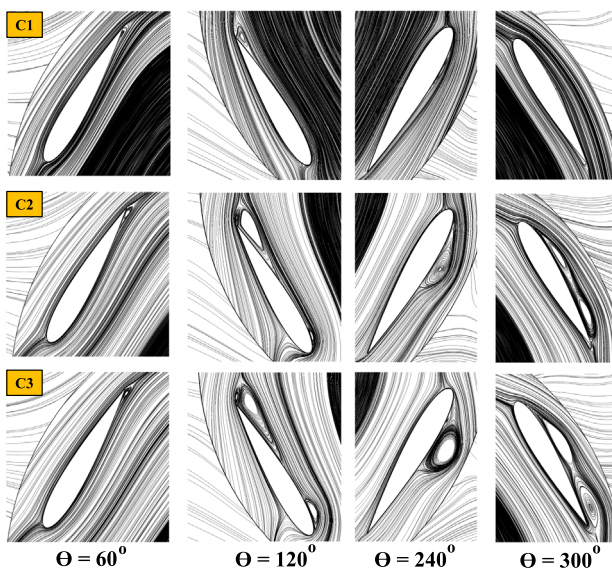

Fig. 16. Instantaneous streamlines around the blade profile at various azimuth angular positions.

the following blades. These vortices separate on each side of the wake, forming a kind of von-Karman street. In the C_1 case, these vortex zones

are smooth lines that take time to disappear. As the upstream velocity increases (C_2), discrete separations of the vortices begin to develop while still maintaining a certain order. For the extreme case (C_3), these separations are much more chaotic, with interaction between the vortices rotating in opposite directions.

The two ending plates cause the flow to be more bi-dimensional between them reducing the vertical drift. In fact, the flow field is quite similar in any section inside the turbine except near the plates. Fig. 19 shows the normalized vorticity fields –corresponding to the C_1 case– around the turbine blades at two different horizontal planes; the upper one at mid-height of the turbine (a), and the lower one near the turbine plate (b). At mid-height, there is no flow separation as the blades rotate, the vortices distribution is very smooth and gradual. The clockwise vortices (negative vorticity values, blue color) separates quite continuously on the left side of the turbine wake (at the top of the figure). However, the counter-clockwise vortices (positive vorticity values, red color) have a discrete pattern with larger vortices separating each time a blade crosses the wake. Close to the plate, the interaction between the vortices of the blades with the plate boundary layer increases the instability. In fact, this interaction generates asymmetric horseshoe-shaped vortices that, on separation, form the main structures of the wake. This can be visualized more clearly in Fig. 20, in which the value of the helicity (the vorticity along the velocity vector) is used to create a three-dimensional image of the horseshoe vortex cloud that forms in the wake of the turbine plates. Although, the vortices generated from the two ending plates seem to increase the complexity and the losses in the wake zone, the plates are very useful from the mechanical point of view to support the turbine blades, and actually improve the hydrodynamic performance. Apart from reducing the blade-tip effects, the plates prevent air from entering the turbine when the surface drops significantly.

5. Conclusions

The performance and the flow field characteristics of a small vertical-axis hydrokinetic turbine inside an open channel have been investigated, through a series of experiments and a free-surface flow analysis, under various operation conditions.

Experimental tests have been carried out for three flow rates with different upstream velocities. It has been found that the peak power coefficients increase with the upstream velocity, and the corresponding tip speed ratios shift to higher values. This effect is directly linked to the blockage ratio and the Froude number. For the higher flow rates (without interference of the free-surface with the turbine), the influence of the Froude number on the power is practically linear.

An intensive three-dimensional multiphase simulation has been carried out to understand the complex free-surface flow around the turbine and its relevance on the overall performance. A reasonably good match has been found between the experimental and the numerical results. The single-phase model values are somewhat higher, as it does not consider the free-surface deformations around the rotor. The VOF model is able to simulate not only the free-surface longitudinal variations, but also the interactions with the channel wall boundaries. The power coefficients obtained are much closer to the experimental ones for the whole range of tip speed ratios. Polar plot diagrams have been used to represent and compare the contribution of each blade on the output torque.

The velocity field around and inside the turbine rotor has been analyzed and correlated with the free-surface variations from upstream to downstream of the turbine. The energy extraction is found to be directly linked to the magnitude of the velocity in the turbine, specifically around the blades, and increasing with the free-surface drop. The surface change is also responsible for the wake recovery behavior.

The relative velocity and the pressure coefficient distribution around the blades have been analyzed with different azimuth angles
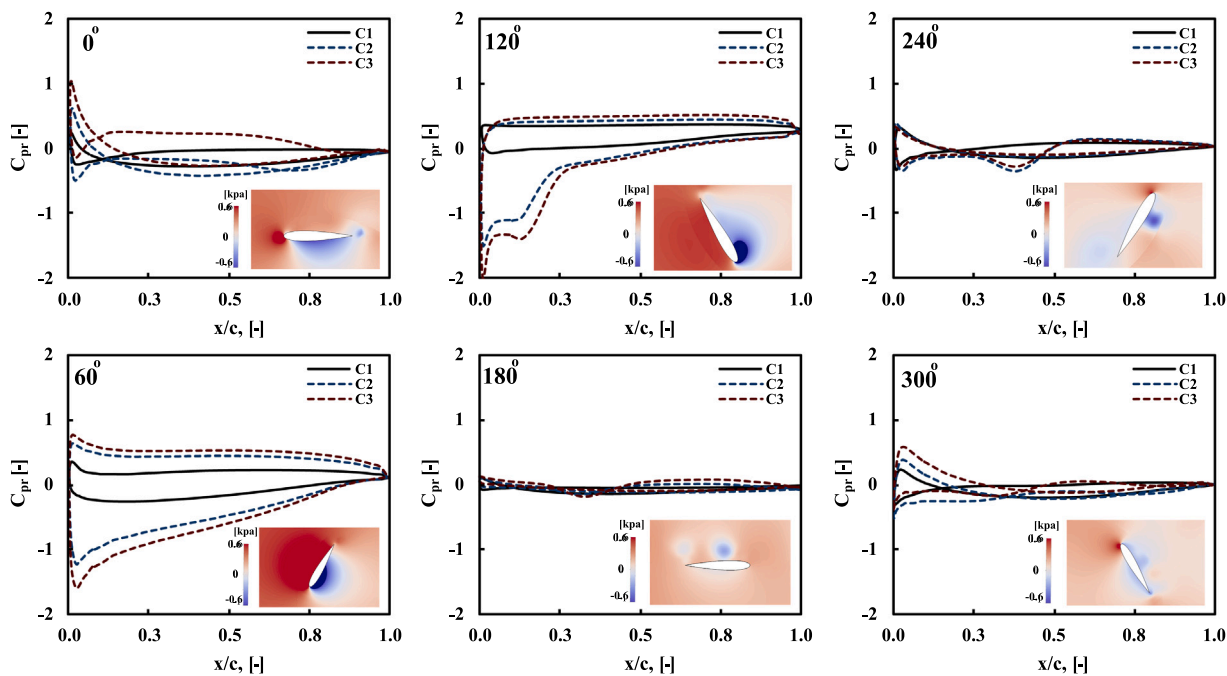
Fig. 17. Pressure coefficient for all cases and pressure contour samples of C_2 on a single blade at $\lambda = 2.3$.
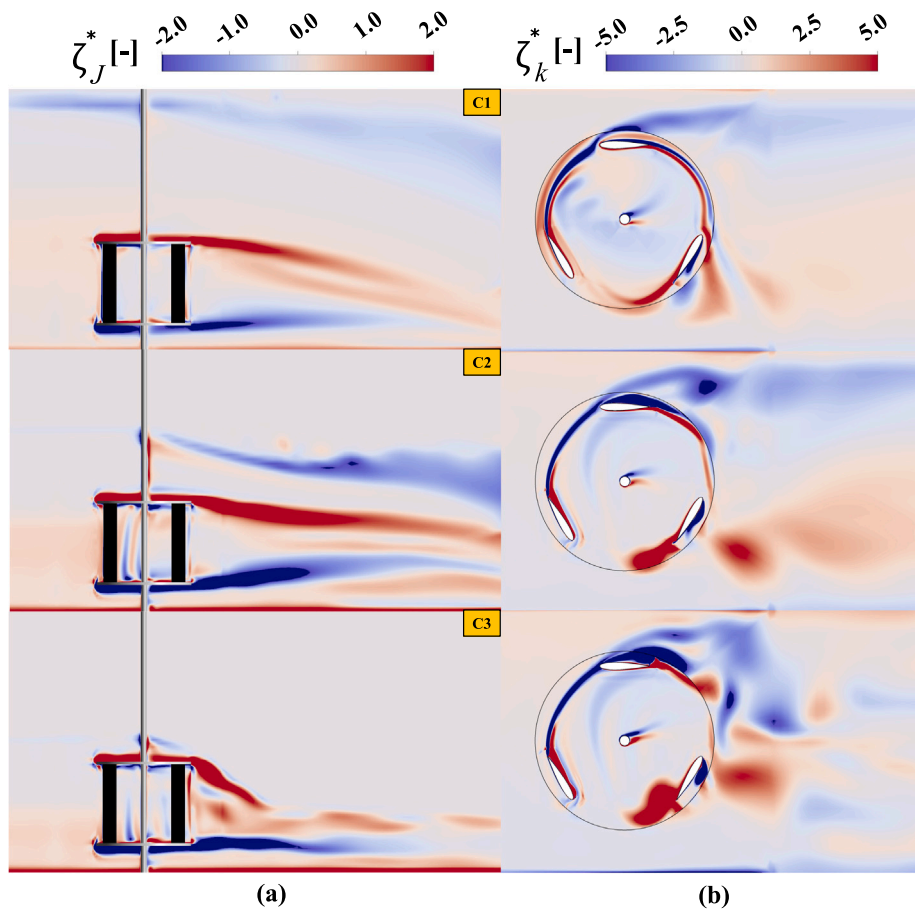

Fig. 18. Normalized vorticity fields $(J - K)$ at the middle sections for all cases.

and have provided a better insight into the positive torque production zones and their relation with the flow separation. An abnormal behavior of the pressure coefficient -a crossover from the pressure to the suction side- have been detected for some cases at specific angular positions. This has been caused by the low pressure zone inside the rotor, due to the high solidity of the blades. The vorticity generated
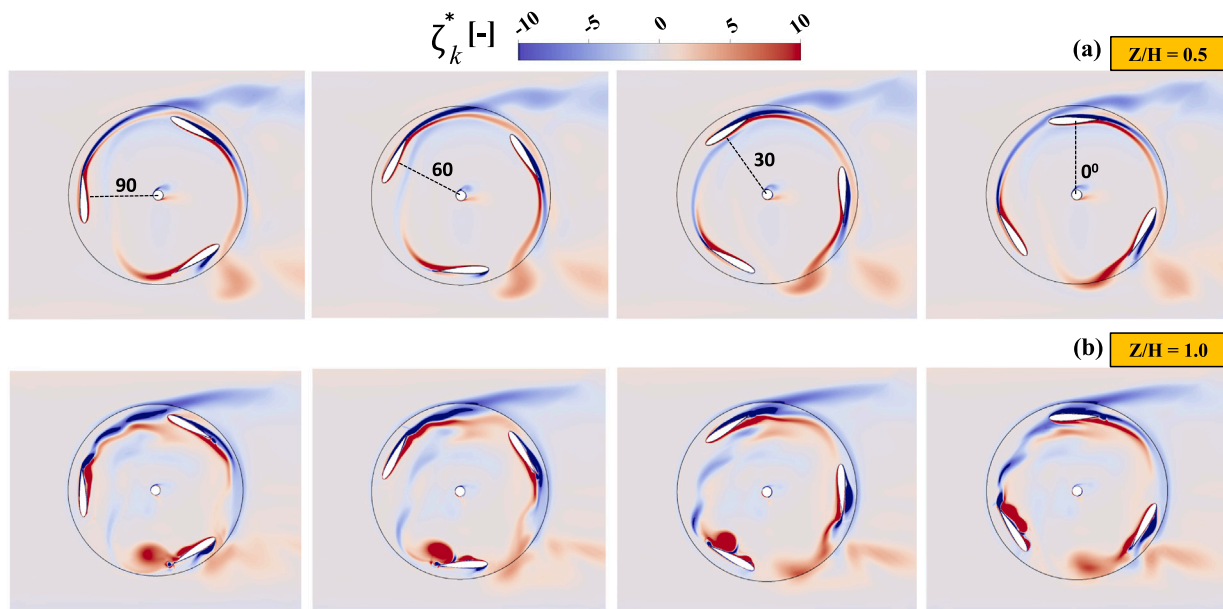
Fig. 19. Normalized vorticity-*K* contours for four angular positions at two different plans at $\lambda = 2.3$.
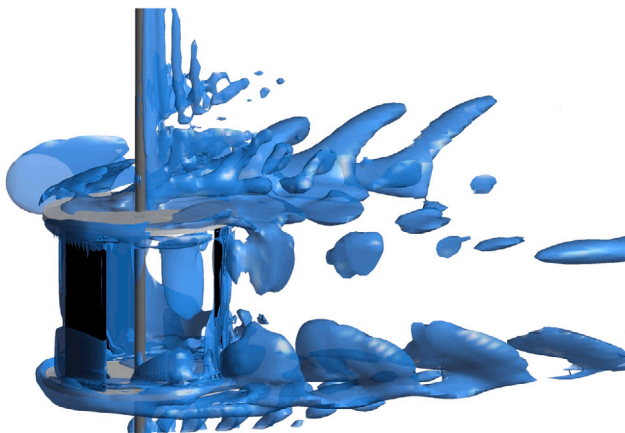

Fig. 20. Absolute helicity showing the horseshoe cloud.

by the blades and the ending plates has been clearly analyzed. The interaction between both of them develops horseshoe vortices that separate from the rotor forming a vortex street.

CRediT authorship contribution statement

Ahmed Gharib Yosry: Conceptualization, Software, Methodology, Writing – original draft. **Eduardo Álvarez Álvarez:** Investigation, Data curation, Review & editing. **Rodolfo Espina Valdés:** Software, Methodology. **Adrián Pandal:** Methodology, Data curation. **Eduardo Blanco Marigorta:** Data curation, Writing – review & editing.

Declaration of competing interest

The authors declare that they have no known competing financial interests or personal relationships that could have appeared to influence the work reported in this paper.

Data availability

Data will be made available on request.

References

[1] J. Gao, H. Liu, J. Lee, Y. Zheng, M. Guala, L. Shen, Large-eddy simulation and Co-Design strategy for a drag-type vertical axis hydrokinetic turbine in open channel flows, Renew. Energy 181 (2022) 1305–1316.

[2] M. Khan, G. Bhuyan, M. Iqbal, J. Quaicoe, Hydrokinetic energy conversion systems and assessment of horizontal and vertical axis turbines for river and tidal applications: A technology status review, Appl. Energy 86 (10) (2009) 1823–1835.

[3] B. Kirke, L. Lazauskas, Limitations of fixed pitch Darrieus hydrokinetic turbines and the challenge of variable pitch, Renew. Energy 36 (3) (2011) 893–897.

[4] M.B. Topper, S.S. Olson, J.D. Roberts, On the benefits of negative hydrodynamic interactions in small tidal energy arrays, Appl. Energy 297 (2021) 117091.

[5] R. Gosselin, G. Dumas, M. Boudreau, Parametric study of H-Darrieus vertical-axis turbines using CFD simulations, J. Renew. Sustain. Energy 8 (5) (2016) 053301.

[6] S.-C. Roh, S.-H. Kang, Effects of a blade profile, the Reynolds number, and the solidity on the performance of a straight bladed vertical axis wind turbine, J. Mech. Sci. Technol. 27 (11) (2013) 3299–3307.

[7] M. Singh, A. Biswas, R. Misra, Investigation of self-starting and high rotor solidity on the performance of a three S1210 blade H-type Darrieus rotor, Renew. Energy 76 (2015) 381–387.

[8] O. Eboibi, L.A.M. Danao, R.J. Howell, Experimental investigation of the influence of solidity on the performance and flow field aerodynamics of vertical axis wind turbines at low Reynolds numbers, Renew. Energy 92 (2016) 474–483.

[9] Y.-L. Xu, Y.-X. Peng, S. Zhan, Optimal blade pitch function and control device for high-solidity straight-bladed vertical axis wind turbines, Appl. Energy 242 (2019) 1613–1625.

[10] F. Jing, Q. Sheng, L. Zhang, Experimental research on tidal current vertical axis turbine with variable-pitch blades, Ocean Eng. 88 (2014) 228–241.

[11] S.M. Camporeale, V. Magi, Streamtube model for analysis of vertical axis variable pitch turbine for marine currents energy conversion, Energy Convers. Manage. 41 (16) (2000) 1811–1827.

[12] D.H. Zeiner-Gundersen, A vertical axis hydrodynamic turbine with flexible foils, passive pitching, and low tip speed ratio achieves near constant RPM, Energy 77 (2014) 297–304.

[13] R. Gupta, A. Biswas, K. Sharma, Comparative study of a three-bucket Savonius rotor with a combined three-bucket Savonius–three-bladed Darrieus rotor, Renew. Energy 33 (9) (2008) 1974–1981.

[14] B. Govind, Increasing the operational capability of a horizontal axis wind turbine by its integration with a vertical axis wind turbine, Appl. Energy 199 (2017) 479–494.

[15] T. Villeneuve, M. Boudreau, G. Dumas, Improving the efficiency and the wake recovery rate of vertical-axis turbines using detached end-plates, Renew. Energy 150 (2020) 31–45.

[16] D. Saeidi, A. Sedaghat, P. Alamdari, A.A. Alemrajabi, Aerodynamic design and economical evaluation of site specific small vertical axis wind turbines, Appl. Energy 101 (2013) 765–775.

[17] C. Shashikumar, V. Madav, Numerical and experimental investigation of modified V-shaped turbine blades for hydrokinetic energy generation, Renew. Energy 177 (2021) 1170–1197.

[18] W.-H. Chen, C.-Y. Chen, C.-Y. Huang, C.-J. Hwang, Power output analysis and optimization of two straight-bladed vertical-axis wind turbines, Appl. Energy 185 (2017) 223–232.

[19] J. Gao, D.T. Griffith, M.S. Sakib, S.Y. Boo, A semi-coupled aero-servo-hydro numerical model for floating vertical axis wind turbines operating on TLPs, Renew. Energy 181 (2022) 692–713.

[20] J.I. Whelan, J. Graham, J. Peiro, A free-surface and blockage correction for tidal turbines, J. Fluid Mech. 624 (2009) 281–291.

[21] G.T. Houlsby, C.R. Vogel, The power available to tidal turbines in an open channel flow, Proc. Inst. Civ. Eng. Energy 170 (1) (2017) 12–21, http://dx.doi.org/10.1680/jener.15.00035.

[22] C. Vogel, G. Houlsby, R. Willden, Effect of free surface deformation on the extractable power of a finite width turbine array, Renew. Energy 88 (2016) 317–324.

[23] C. Vogel, R. Willden, G. Houlsby, Power available from a depth-averaged simulation of a tidal turbine array, Renew. Energy 114 (2017) 513–524.

[24] S. Yagmur, F. Kose, S. Dogan, A study on performance and flow characteristics of single and double H-type Darrieus turbine for a hydro farm application, Energy Convers. Manage. 245 (2021) 114599.

[25] P. Ouro, S. Runge, Q. Luo, T. Stoesser, Three-dimensionality of the wake recovery behind a vertical axis turbine, Renew. Energy 133 (2019) 1066–1077.

[26] N. Guillaud, G. Balarac, E. Goncalves, J. Zanette, Large eddy simulations on vertical axis hydrokinetic turbines-power coefficient analysis for various solidities, Renew. Energy 147 (2020) 473–486.

[27] P. Ouro, T. Stoesser, An immersed boundary-based large-eddy simulation approach to predict the performance of vertical axis tidal turbines, Comput. & Fluids 152 (2017) 74–87.

[28] T. Kinsey, G. Dumas, Impact of channel blockage on the performance of axial and cross-flow hydrokinetic turbines, Renew. Energy 103 (2017) 239–254.

[29] I.A. Tunio, M.A. Shah, T. Hussain, K. Harijan, N.H. Mirjat, A.H. Memon, Investigation of duct augmented system effect on the overall performance of straight blade Darrieus hydrokinetic turbine, Renew. Energy 153 (2020) 143–154.

[30] K. Sun, R. Ji, J. Zhang, Y. Li, B. Wang, Investigations on the hydrodynamic interference of the multi-rotor vertical axis tidal current turbine, Renew. Energy 169 (2021) 752–764.

[31] S. Zanforlin, Advantages of vertical axis tidal turbines set in close proximity: A comparative CFD investigation in the English channel, Ocean Eng. 156 (2018) 358–372.

[32] B. Chen, S. Cheng, T.-c. Su, H. Zhang, Numerical investigation of channel effects on a vertical-axis tidal turbine rotating at variable speed, Ocean Eng. 163 (2018) 358–368.

[33] Y. Nishi, G. Sato, D. Shiohara, T. Inagaki, N. Kikuchi, Performance characteristics of axial flow hydraulic turbine with a collection device in free surface flow field, Renew. Energy 112 (2017) 53–62.

[34] N. Kolekar, A. Banerjee, Performance characterization and placement of a marine hydrokinetic turbine in a tidal channel under boundary proximity and blockage effects, Appl. Energy 148 (2015) 121–133.

[35] J. Yan, X. Deng, A. Korobenko, Y. Bazilevs, Free-surface flow modeling and simulation of horizontal-axis tidal-stream turbines, Comput. & Fluids 158 (2017) 157–166.

[36] A. Benavides-Morán, L. Rodríguez-Jaime, S. Laín, Numerical investigation of the performance, hydrodynamics, and free-surface effects in unsteady flow of a horizontal axis hydrokinetic turbine, Processes 10 (1) (2021) 69.

[37] X. Sun, J. Chick, I. Bryden, Laboratory-scale simulation of energy extraction from tidal currents, Renew. Energy 33 (6) (2008) 1267–1274.

[38] J. Riglin, W.C. Schleicher, I.-H. Liu, A. Oztekin, Characterization of a micro-hydrokinetic turbine in close proximity to the free surface, Ocean Eng. 110 (2015) 270–280.

[39] Y. Nishi, G. Sato, D. Shiohara, T. Inagaki, N. Kikuchi, A study of the flow field of an axial flow hydraulic turbine with a collection device in an open channel, Renew. Energy 130 (2019) 1036–1048.

[40] M. Nakajima, S. Iio, T. Ikeda, Performance of Savonius rotor for environmentally friendly hydraulic turbine, J. Fluid Sci. Technol. 3 (3) (2008) 420–429.

[41] R. Espina-Valdés, A. Fernández-Jiménez, J.F. Francos, E.B. Marigorta, E. Álvarez-Álvarez, Small cross-flow turbine: Design and testing in high blockage conditions, Energy Convers. Manage. 213 (2020) 112863.

[42] Z. Yin, M. Esmaeilpour, The hydrodynamic performance of a turbine in shallow free surface flow, J. Hydrodyn. 33 (4) (2021) 804–820.

[43] A.E.B. Le Hocine, R.J. Lacey, S. Poncet, Multiphase modeling of the free surface flow through a Darrieus horizontal axis shallow-water turbine, Renew. Energy 143 (2019) 1890–1901.

[44] J. Deng, S. Wang, P. Kandel, L. Teng, Effects of free surface on a flapping-foil based ocean current energy extractor, Renew. Energy 181 (2022) 933–944.

[45] M. Claessens, The Design and Testing of Airfoils for Application in Small Vertical Axis Wind Turbines (Master of Science thesis), 2006, Aerospace Engineering.

[46] A. Sengupta, A. Biswas, R. Gupta, Studies of some high solidity symmetrical and unsymmetrical blade H-Darrieus rotors with respect to starting characteristics, dynamic performances and flow physics in low wind streams, Renew. Energy 93 (2016) 536–547, http://dx.doi.org/10.1016/j.renene.2016.03.029, URL https://www.sciencedirect.com/science/article/pii/S0960148116302130.

[47] K.W. Lewis, The Cumulative Effects of Roughness and Reynolds Number on NACA 0015 Airfoil Section Characteristics (Ph.D. thesis), Texas Tech University, 1984.

[48] E. Jacobs, A. Sherman, Airfoil Section Characteristics as Affected by Variations of the Reynolds Number, Report-National Advisory Committee for Aeronautics, (227) US Government Printing Office, 1937, pp. 577–611.

[49] C. Hirt, B. Nichols, Volume of fluid (VOF) method for the dynamics of free boundaries, J. Comput. Phys. 39 (1) (1981) 201–225, http://dx.doi.org/10.1016/0021-9991(81)90145-5, URL https://www.sciencedirect.com/science/article/pii/0021999181901455.

[50] P.J. Roache, Perspective: A method for uniform reporting of grid refinement studies, J. Fluids Eng. 116 (3) (1994) 405–413.

[51] F.R. Menter, Two-equation eddy-viscosity turbulence models for engineering applications, AIAA J. 32 (8) (1994) 1598–1605.

[52] D.C. Wilcox, Reassessment of the scale-determining equation for advanced turbulence models, AIAA J. 26 (11) (1988) 1299–1310.